

Automated Measurement of Highly Divergent Optical Wavefronts with a Scanning Shack-Hartmann Sensor

Martin E. Fuerst, Ernst Csencsics, Nikolaus Berlakovich and Georg Schitter, *Senior Member, IEEE*
Christian Doppler Laboratory for Precision Engineering for Automated In-Line Metrology,
Automation and Control Institute (ACIN), Technische Universität Wien
Vienna, Austria
fuerst2@acin.tuwien.ac.at

Abstract—In this paper, a Shack-Hartmann wavefront sensor (SHS) is combined with a mechatronic positioning system to overcome the limited dynamic range of the SHS by repositioning and reorienting the SHS. Feedback loops to ensure a tangential orientation of the wavefront sensor in every measurement position and a measurement strategy that compensates for tip and tilt between wavefront and sensor are described and implemented. A framework that estimates the admissible measurement trajectories by relating the positioning errors caused by misalignments of the stages to the parameters of the wavefront sensor, is developed. It is demonstrated that the setup is capable of directly measuring a highly divergent optical wavefront by combining wavefront data and positioning data acquired along the wavefront generated by a microscope objective with NA of 0.45.

Index Terms—Shack-Hartmann wavefront sensor, Dynamic range extension, Optical metrology, Automatic optical inspection, Quality management, Error Budgeting

I. INTRODUCTION

Focused light is important in various fields of modern science and industry. Laser material processing requires focused lasers to deposit large amounts of energy in small volumes [1], the resolution of advanced microscopy techniques is increased by a sharper focus [2] and high-precision optical displacement sensors also benefit from small spot sizes [3]. Due to the wave-nature of light, it cannot be arbitrarily focused [4]. The smallest achievable spot size is limited by the numerical aperture of an optical system, which is defined as $NA = n \cdot \sin \alpha$ with n being the refractive index of the medium and α the half opening angle of the focused beam [5] (see also Fig. 1). Optical designers thus strive to maximize the NA when designing for focusing applications. In reality, however, aberrations caused by misalignments or manufacturing errors often degrade the quality of the focused spot [6].

A very common aberration is the *spherical aberration*, which is present in every optical system that consists of spherical lenses, but becomes more problematic with increasing NA [7]. Spherical aberration can be eliminated by utilizing aspherical (parabolic) optics and the emerging field of *freeform* optics is a promising approach to minimize remaining aberrations such as astigmatism, coma, etc. The difficulty with aspherical and freeform optical components, is that they are

much more difficult to manufacture and to align [8]. Also, the quality of freeform parts is more challenging to assess than the quality of classical, spherical focusing optics. However, there is a mutual characteristic [9]: The qualification typically relies on *shape* measurements of the optical component, which are either collected by areal, interferometric methods or single-point-probe based profilometry methods [10].

The interferometric principle is commonly used for testing optical elements with low NA [10], [11]. The benefits are high precision and sub-nm resolution. To measure highly divergent wavefronts, however, null-elements are required, which are either given by a “golden master” reference optic or computer generated holograms (CGHs) [12]. In both cases, the versatility of the measurement tool is greatly reduced as each new surface geometry requires a new null-lens. The null-optic is also an additional source of uncertainty in the measurement process. Further, the interferometric approach suffers from a high vibration sensitivity, which renders it difficult to use it in industrial environments. The profilometric or coordinate-based methods are well suited for nearly any part shape, can be equipped with tactile or non-tactile probes, and offer resolutions comparable to the interferometric approach [10], [13]. Optical parts are typically measured with non-tactile probes, as delicate coatings may be damaged by a tactile probe [14]. Compared to interferometric approaches, CMMs and profilometers are typically much slower, as the surface data has to be acquired point-by-point or line-by-line.

To avoid the drawbacks of shape measurements, it was proposed to directly measure the optical part *performance* [9]. This can be achieved by measuring the shape of the *optical wavefront* that is transmitted or reflected by an optical part or system. A commonly used wavefront sensor is the Shack-Hartmann sensor (SHS), which is a camera-based sensor that measures the shape of an incoming wavefront region in a single shot [15]. As SHS are small, robust, fast and comparatively insensitive to vibrations, they are well suited for industrial environments [16]. Their capability to characterize lenses bigger than the sensor aperture was recently demonstrated [17], [18]. This was done by manual linear repositioning of the sensor and subsequent stitching of the acquired wavefront subaperture

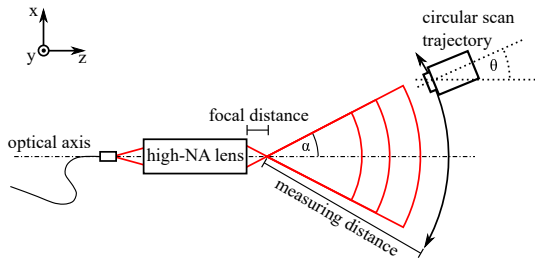


Fig. 1: Scanning wavefront sensor strategy. By increasing the measurement distance, the wavefront curvature is sufficiently reduced to be observable by the Shack-Hartmann sensor. To compensate the incidence angle, the sensor is reoriented (angle θ).

images. However, the SHS is limited when it comes to the measurement of highly divergent wavefronts [19]. This is a problem when evaluating focusing optics, as these require high numerical apertures (NA) to create small, diffraction-limited focal spots. Approaches involving null-optics to enable Shack-Hartmann-wavefront sensing of high-NA lenses were also demonstrated [20], but these also suffer from the necessity of a specific null-optic and its additional uncertainties.

A recently published approach bypasses the limitations of the Shack-Hartmann sensor by mechanically repositioning the sensor along the wavefront [21]. The idea is to increase the measurement distance and thereby reduce the curvature of the incident wavefront on the sensor (see Fig. 1). In this case, only a part of the entire wavefront is observed in a single wavefront image, such that the sensor needs to be moved to multiple positions along the wavefront for collecting a number of partial images (or “subapertures”). The collected data is then interpreted in combination with the positioning data to obtain the complete wavefront. The presented approach uses pre-planned sensor positions and orientations based on the expected wavefront, which limits its applicability to arbitrary optics.

The contribution of this paper is (a) the design of a fully automated scanning SHS system, (b) a measurement procedure to enable automatic tangential alignment, (c) a framework to estimate the systematic positioning errors that limit the admissible trajectory radius, and (d) an experimental validation of the system enabling the direct measurement of highly divergent wavefronts. This paper is an extension of a previously published conference contribution [22] and provides a deeper insight in the system design, the influence of systematic positioning errors caused by misalignment, and their effect on the choice of suitable measurement trajectories. This paper proposes a versatile instrument that allows, without the need for nullifying optical elements, the characterization of optical parts that generate highly divergent wavefronts.

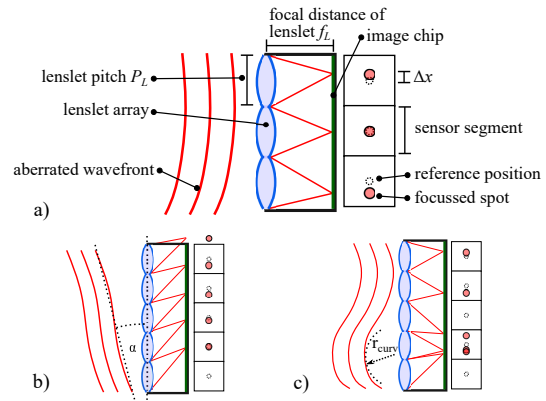


Fig. 2: Principle of a Shack-Hartmann sensor. a) Working principle and labeled components of a SHS. b) For a large global tilt of the incident wavefront, spots leave their assigned sensor regions. c) For large local curvature, multiple spots are registered in the same sensor region.

II. SHACK-HARTMANN WAVEFRONT SENSING

A. Principle

A wavefront of any monochromatic wave phenomenon is defined as a surface that is formed by a set of points of equal phase of the corresponding field strength. A Shack-Hartmann sensor consists of a microlens array and an image sensor and measures the phase distribution of an incident optical wave at the plane of the microlens array [15]. The working principle is illustrated in Fig. 2a. Each microlens produces a focused spot on the image sensor, the position of the spot being dependent on the average slope of the wavefront segment incident on the microlens. From the recorded spot pattern, local slopes can be calculated via

$$\tan(\alpha) = \frac{\Delta x}{f_L} \quad (1)$$

with Δx the displacement of a spot from its reference position, f_L the focal length of the lenslet and α the wavefront slope (adapted from [23]). The local slope map is then used to reconstruct the wavefront shape [15]. Shack-Hartmann sensors offer a high measurement speed, are relatively robust to vibrations and have sub-wavelength resolution down to 0.01λ [16].

B. Limitations of the Shack-Hartmann sensor

Two wavefront characteristics limit the Shack-Hartmann sensor's dynamic range: wavefront slope and wavefront curvature [19].

Wavefront slope describes the average angle between the incident wavefront and the sensor aperture. The SHS measures wavefront shape by relating the shift of the spot pattern to the incidence angle, as given in (1). When the shift exceeds half the lenslet pitch, the focused spots leave their assigned sensor region (see Fig. 2b)), which prevents unambiguous assignment of spot to lenslet. To ensure that spots are registered within

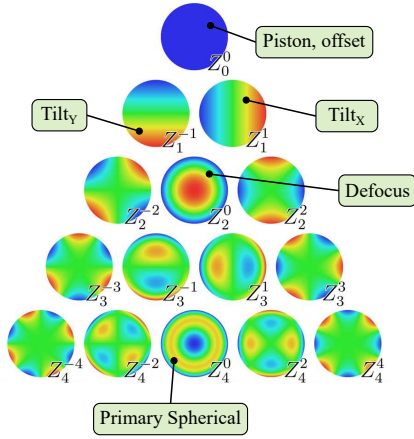


Fig. 3: First 15 Zernike polynomials and the related optical aberrations.

their respective sensor regions, the maximum admissible incidence angle is limited to

$$\alpha_{max} = \frac{P_L}{2 \cdot f_L}, \quad (2)$$

with lenslet pitch P_L as in Fig. 2a. For typical Shack-Hartmann sensor parameters ($P_L = 100 - 200 \mu\text{m}$, $f_L = 3 - 10 \text{ mm}$), α_{max} is only a few degrees ($1-5^\circ$). This limit can be extended to about $10-15^\circ$ by advanced spot assignment techniques, but with increasing incidence angle, aberrations caused by the lenslets reduce the sensor's accuracy.

Wavefront curvature describes the local variation of the wavefront slope and can be characterized by the radius of curvature r_{curv} . When r_{curv} is below a certain threshold, and the curvature is thus too high, multiple spots are formed in the same segment of the sensor, making the assignment of spot to lenslet ambiguous (see Fig. 2c). The minimal acceptable r_{curv} depends on wavelength (due to diffraction limited spot sizes), but is typically given by $r_{curv} \geq 3 \cdot f_L$. Efforts to solve this problem by advanced spot assignment algorithms have been reported, e.g. by [24]. However, these algorithms typically rely on prior knowledge of the main encountered aberrations and cannot compensate for the optical degradations that also accompany high curvatures and slopes incident on the sensor.

These limitations impede the direct assessment of a highly-divergent wavefront with a single, static SHS.

C. Zernike decomposition

The Zernike polynomials Z_n^m are a set of base polynomials that are orthogonal on the unit disk [25]. They are commonly used in optometry, ophthalmology and adaptive optics because the individual polynomials can be related to typical aberrations from optics theory, such as the Seidel aberrations. Any

wavefront $W(\rho, \phi)$ (with radial coordinates ρ, ϕ) on a spherical aperture can thus be decomposed into its Zernike components.

$$W(\rho, \phi) = \sum_{m,n} [a_{m,n} Z_n^m(\rho, \phi) + b_{m,n} Z_n^{-m}(\rho, \phi)] \quad (3)$$

The coefficients $a_{m,n}$, $b_{m,n}$ are referred to as Zernike coefficients. Figure 3 displays graphical representations of the first 15 Zernike polynomials Z_n^m in the standard ordering (by radial degree n and azimuthal degree m). The polynomials corresponding to aberrations important for this paper are labeled accordingly.

III. SCANNING SHACK-HARTMANN SENSOR SYSTEM

A. Concept

The limitations of a single, static SHS when used to measure highly divergent wavefronts (as described in Section II-B) can be summarized like this: When the sensor is placed close to the focus point, the curvature incident on the sensor is too high, when placed far away, only a part of the wavefront is measured.

To successfully perform a wavefront measurement on a highly-divergent optic without using a nullifying element (and thus avoiding additional cost, inconvenience and aberration), a scanning Shack-Hartmann sensor (scanning-SHS) system is developed. By increasing the measurement distance and *scanning along the wavefront* generated by the optic under test, the limitations of a static SHS can be avoided (see Figure 1). A pure translational scan perpendicular to the optical axis would result in high incidence angles at the outer positions, again exceeding the dynamic range of the Shack-Hartmann sensor. By reorienting the sensor tangentially to the wavefront, the incidence angle and the curvature can be kept within limits. Effectively, the opening angle α of the focusing optic is compensated by the mechanical stage angle θ to enable a wavefront measurement.

In static SHS setups, the exit pupil of the optical system under test is imaged onto the SHS's lenslet array with an optical relay system, typically comprised of a Keplerian telescope. This serves two purposes: (i) matching of the beam diameter and the SHS aperture diameter, (ii) conjugating the planes of the lenslet array and the optic under test's exit pupil. When these conditions are met, no further data processing is necessary to compare wavefront measurement data between different measurement setups. To directly compare the wavefront measurement data acquired with the *Scanning* SHS to conventionally acquired wavefront images, the wavefront needs to be numerically propagated to the exit pupil of the optic under test. This is possible with the positioning data available from the positioning system. Further, due to the absence of a nullifying optic, the divergent wavefront data itself contains information about its position in space. For instance, the recorded curvature radius indicates the wavefront's distance from its focal point.

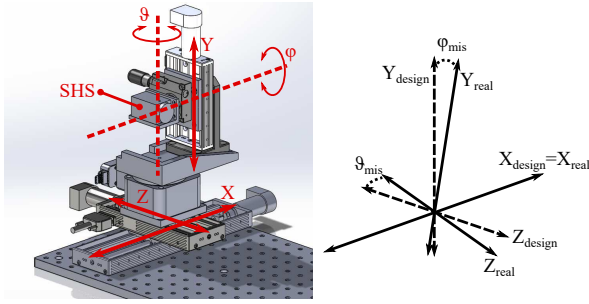


Fig. 4: The layout of the positioning system.

B. System design

To fully scan a spherical wavefront, a positioning system with five degrees of freedom is required. A rotation around the optical axis of the sensor does not provide additional benefits for the Scanning Shack-Hartmann approach and can thus be omitted. The SHS needs to be positioned in 3 dimensions and oriented in 2 dimensions, such that 3 translational and 2 rotational degrees of freedom are necessary.

This can be achieved with a variety of serial or parallel kinematic layouts. While parallel kinematics typically offer advantages, such as avoiding accumulating positioning errors due to tolerance stack-up, high stiffness and higher speed, their forward kinematics are more difficult to compute, calibration is more cumbersome and the realized workspaces are smaller [26]. In contrast, serial kinematics offer large workspaces, simple calibration and easy computation of the forward kinematics, which makes them well-suited for prototype setups.

Figure 4 shows the designed system, chosen for simplicity of the resulting kinematics. Two linear stages are mounted on top of each other for movement in x- and z-direction (with z being the optical axis parallel to the optical table). On top of the x/z-stages, the ϑ -rotational stage is mounted such that its axis of rotation is orthogonal to the x/z-plane. The y-stage is mounted on the ϑ -stage and the φ -stage is mounted on the y-stage. Finally, the Shack-Hartmann sensor is attached to the φ -stage. In this configuration, the mounting plates can be dimensioned in such a way that the axes of rotation of the ϑ - and the φ -stages intersect the center of the SHS's lenslet array. This also keeps the linear positioning (x/y/z) coordinates independent of the rotational (ϑ/φ) coordinates.

C. Error estimation

The scanning SHS approach relies on the combination of wavefront sensor data and positioning data to accurately reconstruct the global wavefront. While the individual uncertainties (resolution, repeatability) of readily available off-the-shelf linear stages and rotational stages are in the range of single micrometers and microradians ([27], [28]), the layout of the proposed scanning setup involves multiple stages mounted on top of each other, resulting in positioning errors caused by misalignments. The rotational stages are only responsible

for tangential orientation of the SHS, while the absolute position uncertainty caused by misalignments of the linear stages increases with the size of the measurement trajectory. For a first order estimation of how these misalignments limit the admissible trajectories, the influence of imperfect angular alignment of the linear stages is thus considered (compare Figure 4). The following equations describe the translational positioning errors caused by stage misalignments:

$$\Delta x = z \cdot \sin \vartheta_{mis} - y \cdot \sin \vartheta \cdot \sin \varphi_{mis} \quad (4a)$$

$$\Delta y = -y \cdot (1 - \cos \varphi_{mis}) \quad (4b)$$

$$\Delta z = -z \cdot (1 - \cos \vartheta_{mis}) - y \cdot \cos \vartheta \cdot \sin \varphi_{mis}, \quad (4c)$$

with ϑ_{mis} defined as the misalignment between x- and z-axis and φ_{mis} as the misalignment of the y-axis relative to the x/z-plane. These equations can be evaluated for an arbitrary trajectory. Since the measurement procedure introduced in Section IV works with circular trajectories, all following considerations assume circular trajectories. Figure 5 displays the results for an exemplary wavefront with $NA = 0.5$, measured with $r_{meas} = 100$ mm at a y-position of 25 mm, assuming misalignments of $\vartheta_{mis} = \varphi_{mis} = 0.5^\circ$. Apart from Δx , Δy and Δz , the geometrical distance $d = \sqrt{\Delta x^2 + \Delta y^2 + \Delta z^2}$ is also shown. The maximum total positioning error (given as the largest value of d along the trajectory) is the critical number, since it limits the reliability of the reconstruction of the global wavefront.

Figure 6 displays d_{max} , the maximum total error, for a number of different circular trajectories, characterized by the NA of the lens and the trajectory radius. It can be seen that with increasing NA and measurement radius, the maximum total error increases quickly and exceeds the uncertainties of the individual stages.

To reliably measure a wavefront with a scanning Shack-Hartmann sensor, the maximum total error d_{max} should not exceed the width of a lenslet (lenslet pitch P_L). This is because the lenslet pitch determines the spacing of the sampled data of the sensor and the stitching algorithms (see Sec. IV-A) rely on detectable lateral features to accurately reconstruct the global wavefront. At the same time, the width of the sensor's aperture ap and the maximum acceptable incidence angle α_{max} require a minimum measurement distance of

$$r_{min} = \frac{ap}{2 \cdot \tan(\alpha_{max})}. \quad (5)$$

In Figure 7, these two limits are calculated for a typical SHS (Optocraft HR-2) and different stage misalignment values ($\vartheta_{mis} = \varphi_{mis}$). The sensor's aperture $ap = 6$ mm, its acceptance angle is about 5° and its lenslet pitch $P_L = 130$ μ m. It can be seen that an increasing misalignment severely limits the allowable trajectory radius. In combination with the (constant) lower boundary given by r_{min} , the maximum NA that can be reliably measured with the scanning SHS system is limited. Reducing the aperture size would reduce the wavefront measurement errors related to the incidence angle on the SHS, but increase the number of required subaperture measurements.

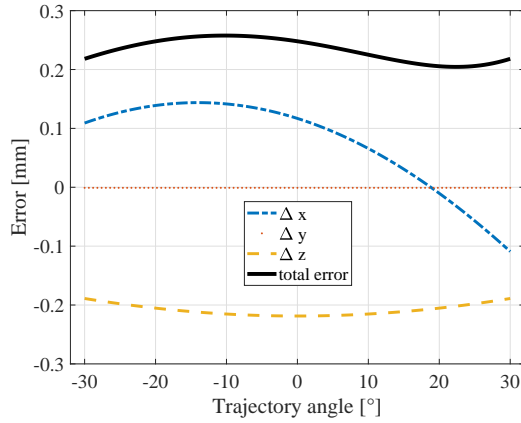


Fig. 5: Errors along a single trajectory. $NA = 0.5 (\pm 30^\circ)$, $r = 100$ mm, $y = 25$ mm, $\vartheta_{mis} = \varphi_{mis} = 0.5^\circ$

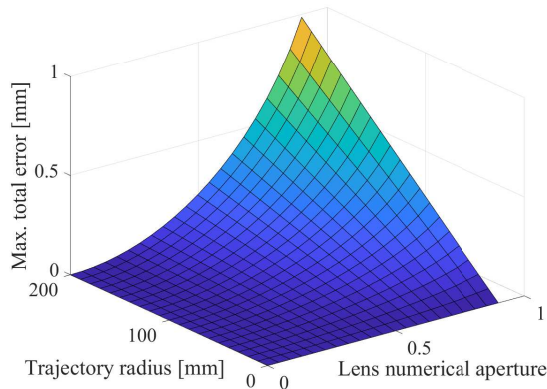


Fig. 6: The maximum total positioning error for multiple circular trajectories.

IV. MEASUREMENT STRATEGY

To automate the setup, the measurement procedure shown in Fig. 8 is implemented. First, the rotational stages are set to 0° , so that the Shack-Hartmann sensor axis is roughly parallel to the optical axis of the system. Then, the sensor is automatically moved perpendicular to the optical axis in x- and y-direction (refer to Fig. 10). After every step, a wavefront measurement is recorded and the $Tilt_X$ - and $Tilt_Y$ - Zernike coefficients are extracted. From the size of these coefficients, the size and direction of the next step are calculated. This is repeated until the values of the $Tilt_X$ - and the $Tilt_Y$ -component are below a fixed threshold value, which is chosen in the system design step. The threshold is given by the positioning resolution of the rotational stages and the sensor noise of the SHS.

After these steps, the sensor is positioned orthogonal to the wavefront, though not necessarily parallel to the optical axis of

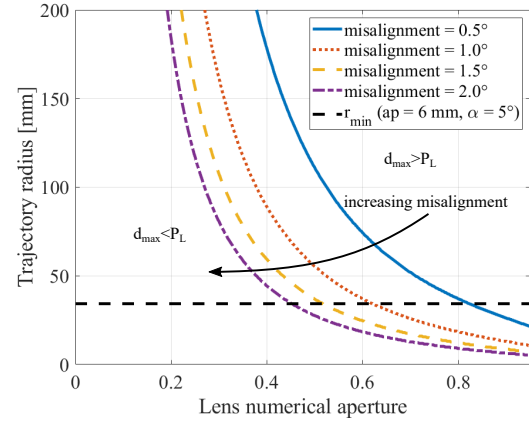


Fig. 7: The boundary line between regions where the error is below or above the threshold value of one lenslet pitch $P_L = 0.13$ mm.

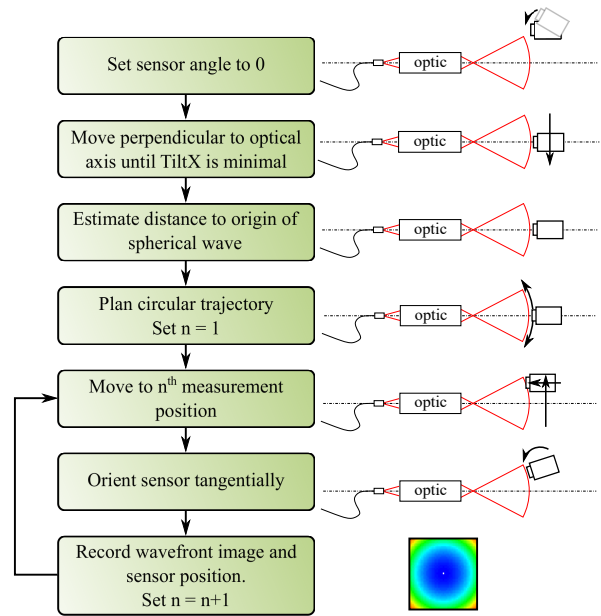


Fig. 8: Flowchart of the fully automated measurement strategy. After initial alignment and reaching the starting position, a trajectory is planned and at each measurement position, the sensor is automatically oriented tangentially to the wavefront.

the optic under test, and its position is recorded as x_0, y_0, z_0 . In this position, another wavefront image is recorded and the wavefront radius r_{est} is calculated from the $Defocus$ Zernike coefficient. A grid of measurement positions, arranged on a sphere, is calculated from the estimated wavefront radius r_{est} , scan range θ_{max}, ϕ_{max} and step sizes $\theta_{step}, \phi_{step}$. The scan range is chosen to match the NA of the optic

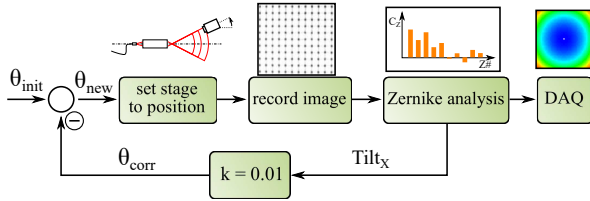


Fig. 9: Flowchart of the feedback loops employed in the measurement strategy. The recorded wavefront is decomposed into its constituent Zernike modes. The $Tilt_X$ component is then used to recalculate the desired ϑ -position. The $Tilt_Y$ component is compensated by an identical loop acting on φ .

under test ($\theta_{max} = \phi_{max} = \arcsin(NA)$) and the step size $\theta_{step} = \phi_{step} = (1 - ov) \cdot \frac{ap}{r_{est}}$ is calculated from the sensor aperture ap , the trajectory radius and the size of the overlap ov between adjacent measurements. With these parameters, the grid coordinates are calculated as:

$$\varphi_j = -\varphi_{max} + (j - 1) \cdot \varphi_{step} \quad (6a)$$

$$\vartheta_i = -\vartheta_{max} + (i - 1) \cdot \vartheta_{step} \quad (6b)$$

$$x_{i,j} = x_0 + r_{est} \cdot \cos(\varphi_j) \cdot \sin(\vartheta_i) \quad (6c)$$

$$y_{i,j} = y_0 + r_{est} \cdot \sin(\varphi_j) \quad (6d)$$

$$z_{i,j} = z_0 + r_{est} \cdot (\cos(\vartheta_i) \cdot \cos(\varphi_j) - 1). \quad (6e)$$

The sensor is moved to one measurement position after the other and is automatically oriented tangentially to the wavefront after every step by minimizing the $Tilt_X$ - and $Tilt_Y$ -components (see Fig. 9). From the automatically preplanned trajectory, the rotational stages orient the sensor to the initial angles $\vartheta_{init} = \vartheta_i, \varphi_{init} = \varphi_j$. A wavefront image is recorded and the $Tilt_X$ and $Tilt_Y$ Zernike coefficients are extracted. The coefficients are multiplied by a factor k and subtracted from $\vartheta_{init}, \varphi_{init}$, resulting in $\vartheta_{new}, \varphi_{new}$. The rotational stages move to $\vartheta_{new}, \varphi_{new}$ and the process is repeated until the observed $Tilt_X$ and $Tilt_Y$ are again below the threshold value described in the initial alignment step. The factor k is determined in a preliminary experiment (data not shown) as the inverse value of the linear relation between positioning angle ϑ and observed $Tilt_X$ coefficient. This essentially equals feedback control with an integrator, such that the obtained value for k is reduced by 30% to add a safety margin to avoid overshoot.

A. Wavefront stitching

With the setup, a number of wavefront images, referred to as *subapertures*, is recorded. As the sensor position is known for each subaperture, the wavefront data can be transformed to its corresponding position in a global laboratory system. Due to mechanical uncertainties and sensor misalignments, the subapertures might deviate from their correct positions causing errors in the wavefront reconstruction. The measurement trajectory is chosen to keep the systematic positioning errors smaller than the lenslet pitch by limiting the trajectory

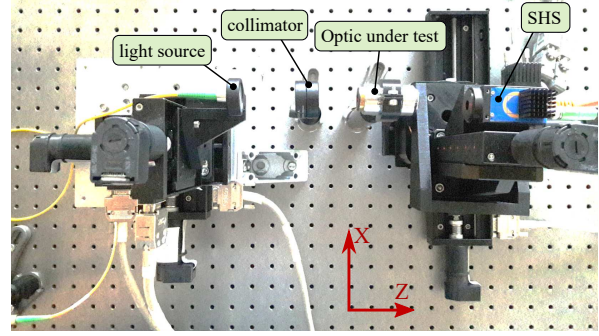


Fig. 10: The presented experimental setup as constructed in the laboratory.

radius (see Sec. III-C). The measurement positions along the trajectory are spaced by half the subaperture diameter, to ensure a sufficiently large overlap region between neighbouring subapertures. To compensate for the remaining misalignments and reconstruct the wavefront, a stitching algorithm is used. The algorithm is based on the ICP (iterative closest point) algorithm which is widely used to match pointclouds and has been used for optical wavefronts [29]. Starting with the central subaperture, neighbouring subapertures are added one by one. From the positioning data and the subaperture size, the overlap region is identified and corresponding points within this region are identified. The squared sum of the distances between corresponding points is minimized by a rigid body transformation of the newly added subaperture. This process is iterated until the difference between the squared sum before and after the last transformation is below the termination condition.

V. SETUP IMPLEMENTATION

To verify the concept of the fully automated scanning-SHS measurement system, an experimental automatic setup consisting of three translational stages and one rotational stage is designed. This four degree-of-freedom setup enables a scanning along a horizontal trajectory in space. The setup follows the layout described in Section III-B, except for the φ -stage, which is omitted for the tests on circular trajectories for reasons of simplicity. Figure 10 shows the setup as realized in the lab. The x-axis is mounted on the optical table, the z-axis is mounted on top of the x-axis. The rotation stage is mounted onto the x-z-stack and the y-stage is mounted on top of the rotation stage. The Shack-Hartmann sensor is mounted onto the y-stage.

The position-controlled linear stages (VT-80 stages from PI Physik Instrumente, Braunschweig, Germany) have a resolution of 500 nm and bidirectional repeatability of 10 μ m. Maximum travel range in the X-, Y- and Z-direction is 200, 50 and 100 mm, respectively. The ϑ -rotation stage (RM-3 model from Newmark Systems Inc., California) offers continuous rotation, a resolution of 1.4 μ rad and a bidirectional repeatability of 218 μ rad. The Shack-Hartmann Sensor (HR-2 model from

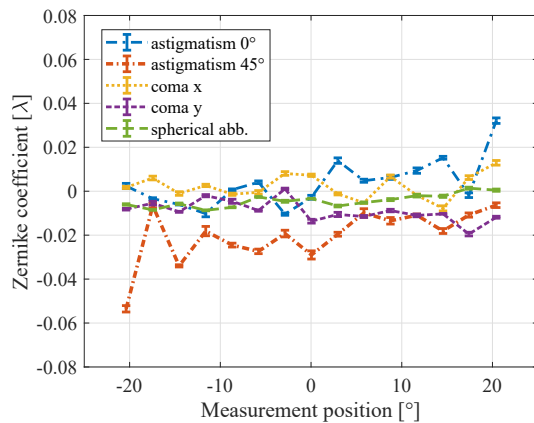


Fig. 11: Results of the repeatability measurements. Mean values and standard deviations of sub aperture Zernike coefficients over 100 runs are shown. The sensor was set to 15 positions on a horizontal, circular trajectory from -21° to $+21^\circ$ degrees and automatically self-aligned in each position.

Optocraft, Erlangen, Germany) has 85×53 lenslets arranged on a rectangular grid with $130 \mu\text{m}$ pitch. Its measurement rate is up to 20 Hz and is calibrated for red light with the wavelength $\lambda = 635 \text{ nm}$ to provide an off-the-shelf resolution of 0.01λ . Its focal length is 3.346 mm , suggesting a maximum incident wavefront angle of 1.13° (following Eq. 2). Through an advanced spot-assignment algorithm, the sensor actually accepts angles up to 10° , which is, however, still insufficient for the high-NA optics modern high-performance applications require.

A. Repeatability of self-alignment

To evaluate the mechanical stability of the scanning setup and the reliability of the feedback loops, measurements on a wavefront generated by an Olympus DPlan 10x microscope objective illuminated by the uncollimated end of a single-mode-fiber-coupled 635 nm laser diode are performed. The variation between the acquired subapertures is evaluated by comparing the Zernike components extracted from the subapertures for 100 runs. In each run, the sensor is moved along the same trajectory but self-aligned anew in each position. Figure 11 shows the results of these measurements. The uncertainties already include the influences of the mechanical stage uncertainties. The variation in the recorded low- and high-order Zernike coefficients is below the sensor resolution of 0.01λ , which justifies the assumption that a repeatable wavefront measurement can be conducted after automated self-alignment.

VI. EXPERIMENTS AND DISCUSSION

To demonstrate the measurement capabilities of a fully automated, scanning Shack-Hartmann sensor setup, the wavefront created by a Motic 20x microscope objective (EC Plan, NA

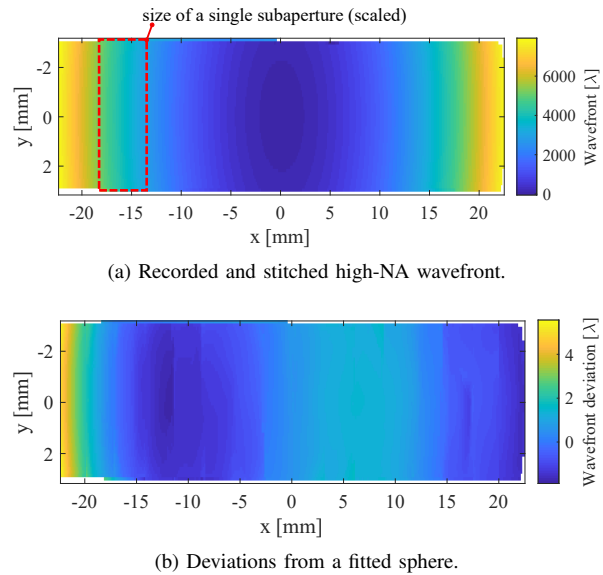


Fig. 12: Result of an automatic wavefront measurement along a circular trajectory. a) Stitched subapertures, the size of a single subaperture image is marked by a red rectangle. b) Remaining shape after subtraction of a fitted sphere.

0.45, corrected for infinity and 0.17 mm specimen cover glass) is investigated. The objective is illuminated by the collimated exit of a fiber-coupled 635 nm laser diode. These first results are obtained with the setup described in Section V, measuring along a single, horizontal circle.

A. Measurement on highly divergent wavefront

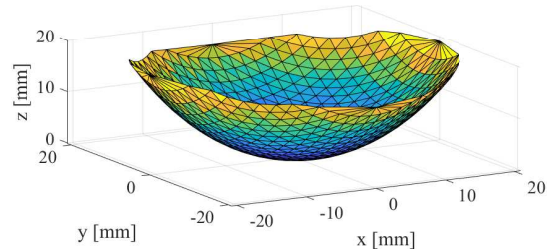
A scan over the full opening angle of the objective ($\text{NA} = 0.45 \rightarrow \alpha = \pm 26.74^\circ$) is performed in 15 steps. From the framework presented in Section III-C, a trajectory radius of 54 mm is chosen, which is above the required r_{\min} and below the threshold above which significant misalignment artifacts are expected.

Figure 12a displays the resulting stitched wavefront. The stitched wavefront is projected along the optical axis into the XY-plane to resemble the commonly used wavefront images of a single, static Shack-Hartmann sensor. The general wavefront shape matches the expectations and is automatically acquired and stitched even though the divergence of the wavefront exceeds the measurement range of the Shack-Hartmann sensor by far.

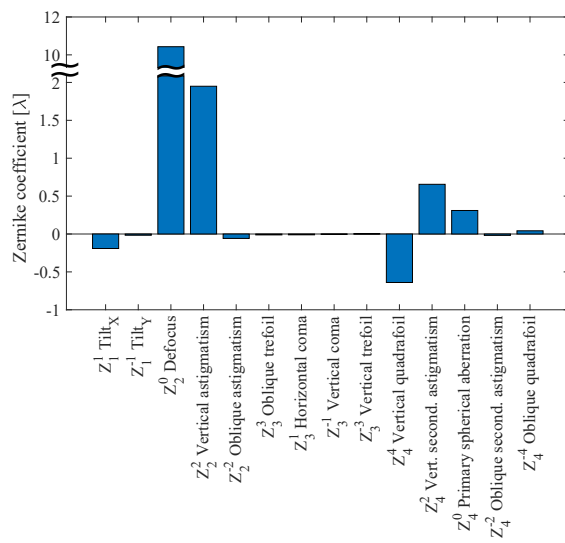
To evaluate the quality of an optic under test, the measured wavefront has to be compared to the desired or the design wavefront. For a focusing optic, such a reference wavefront closely resembles a sphere, therefore a sphere is fitted to the measurement data as a first reference. Figure 12b presents the deviations of the measured wavefront from the fitted sphere. The rms-deviation from the sphere is 1.32λ or $0.84 \mu\text{m}$. This rather large deviation may be explained by the absence of the

microscope coverslip, which the objective is designed to be used with.

B. Zernike reconstruction of global wavefront



(a) 3D plot of a computed wavefront that fits the measurement data.



(b) Zernike coefficients of the reconstructed wavefront.

Fig. 13: A Zernike wavefront is fitted to the measurement data. a) 3D representation of the global wavefront. b) Zernike coefficients of the reconstructed wavefront.

The collected data can also be used to fit a global wavefront from Zernike polynomials. Figure 13a displays a 3D representation of the fitted wavefront. Figure 13b presents the Zernike coefficients that make up the wavefront shown in Fig. 13a. The $Tilt_x$ - and $Tilt_y$ -components are close to zero while the $Defocus$ -component is quite pronounced, as is expected from the focusing optic under test and the setup of the experiment. The higher-order aberrations are indicators for the quality of the optical component. The main components measured are *Vertical astigmatism* (primary and secondary), *Vertical quadrafoil* and *Primary spherical* aberrations.

In summary, it is demonstrated that the fully automated, self-aligning scanning Shack-Hartmann sensor enables measurement of a highly divergent wavefront by stitching a set

of recorded subapertures. A framework for estimating the admissible trajectories based on the positioning errors caused by stage misalignments and relating them to the SHS parameters, is developed and the reliability of the positioning data, which are needed in combination with the recorded wavefront data, is confirmed by repeatability experiments.

VII. CONCLUSION

In this paper, a measurement system based on the concept of a self-aligning scanning Shack-Hartmann sensor is designed and implemented in order to obtain measurements on highly-divergent wavefronts. A framework is established that allows to estimate which optical parts can be reliably measured with the system, considering that alignment errors are to be expected.

Within these limitations, the repeatability of the self-alignment procedure is investigated, with the remaining sub-aperture image uncertainties being within the range of the Shack-Hartmann sensor accuracy. The measurement of a wavefront with a numerical aperture of 0.45 (corresponding to an opening angle of $\pm 26^\circ$) is recorded by automatic repositioning and orienting of a Shack-Hartmann sensor and subsequent stitching of the individual subapertures.

Two ways of analyzing the resulting global wavefront image are explored: Subtraction of a spherical reference surface from the measurement data and decomposition of the recorded surface into its Zernike components. Further research is primarily aimed at identifying the benefits and drawbacks of the evaluation strategies for different use cases. The comparison with a reference surface is an indicator for optical component quality and may thus be used in manufacturing of optical elements while the Zernike decomposition can serve as an indicator for optical system alignment and may be employed in automatic alignment schemes.

Further work is aimed at testing the concept with a full, 5-DoF-setup on a wider variety of focusing optics and on establishing a procedure to correlate the wavefront measurements acquired with the scanning system to optical surface characteristics. In combination with advanced stitching algorithms, measurements on reference artifacts will be compared to results acquired with established measurement techniques such as interferometry.

ACKNOWLEDGMENT

We thank Johannes Schlarp and Shingo Ito from ACIN at TU Wien as well as Johannes Pfund, Ralf Dorn and Christian Brock from Optocraft GmbH for their support and fruitful discussions. The financial support by the Christian Doppler Research Association, the Austrian Federal Ministry for Digital and Economic Affairs, and the National Foundation for Research, Technology and Development, as well as MICRO-EPSILON MESSTECHNIK GmbH & Co. KG and ATENSOR Engineering and Technology Systems GmbH is gratefully acknowledged.

REFERENCES

- [1] J. D. Majumdar and I. Manna, "Laser material processing," *International Materials Reviews*, vol. 56, no. 5-6, pp. 341-388, nov 2011.
- [2] S. W. Hell, S. J. Sahl, M. Bates, X. Zhuang, R. Heintzmann, M. J. Booth, J. Bewersdorff, G. Shtengel, H. Hess, P. Tinnefeld *et al.*, "The 2015 super-resolution microscopy roadmap," *Journal of Physics D: Applied Physics*, vol. 48, no. 44, p. 443001, 2015.
- [3] X. Zou, X. Zhao, G. Li, Z. Li, and T. Sun, "Non-contact on-machine measurement using a chromatic confocal probe for an ultra-precision turning machine," *The International Journal of Advanced Manufacturing Technology*, vol. 90, no. 5-8, pp. 2163-2172, oct 2016.
- [4] B. E. Saleh and M. C. Teich, *Fundamentals of photonics*. John Wiley & sons, 2019.
- [5] M. Born and E. Wolf, *Principles of optics: electromagnetic theory of propagation, interference and diffraction of light*. Elsevier, 2013.
- [6] M. Scaggs and G. Haas, "Optical alignment influenced aberrations in laser beam delivery systems and their correction," in *Laser Resonators, Microresonators, and Beam Control XVII*, A. V. Kudryashov, A. H. Paxton, V. S. Ilchenko, L. Aschke, and K. Washio, Eds. SPIE, 2015.
- [7] R. E. Fischer, B. Tadic-Galeb, P. R. Yoder, R. Galeb, B. C. Kress, S. C. McClain, T. Baur, R. Plympton, B. Wiederhold, and B. G. A. J. *Optical System Design, Second Edition*. McGraw-Hill, SPIE Press, 2008, vol. PM176.
- [8] F. Lamontagne, U. Fuchs, M. Trabert, and A. Möhl, "Aspheric lens mounting," *International Optical Design Conference 2017*, vol. 57, no. 10, p. 7, 2017.
- [9] F. Z. Fang, X. D. Zhang, A. Weckenmann, G. X. Zhang, and C. Evans, "Manufacturing and measurement of freeform optics," *CIRP Annals - Manufacturing Technology*, vol. 62, no. 2, pp. 823-846, 2013.
- [10] S. Chen, S. Xue, D. Zhai, and G. Tie, "Measurement of freeform optical surfaces: Trade-off between accuracy and dynamic range," *Laser & Photonics Reviews*, vol. 14, no. 5, p. 1900365, 2020.
- [11] B. C. Kim, T. Saig, Q. Wang, J. Soons, R. S. Polvani, and U. Griesmann, "The Geometry Measuring Machine (GEMM) Project at NIST," *Proceedings of the 2004 ASPE Winter Top. Meeting, North Carolina, USA*, pp. 3-6, 2004.
- [12] J. H. Burge, "Applications of computer-generated holograms for interferometric measurement of large aspheric optics," in *International Conference on Optical Fabrication and Testing*, vol. 2576. International Society for Optics and Photonics, 1995, pp. 258-269.
- [13] G. Dai and B. Sebastian, "A high precision micro / nano CMM using piezoresistive tactile probes," 2009.
- [14] R. Henselmans, L. A. Cacace, G. F. Y. Kramer, P. C. J. N. Rosielle, and M. Steinbuch, "The NANOMEFOS non-contact measurement machine for freeform optics," *Precision Engineering*, vol. 35, no. 4, pp. 607-624, 2011.
- [15] B. C. Platt and R. Shack, "History and Principles of Shack-Hartmann Wavefront Sensing," *Journal of Refractive Surgery*, vol. 17, no. 5, pp. S573-S577, 2001.
- [16] M. Thier, R. Paris, T. Thurner, and G. Schitter, "Low-latency shack-hartmann wavefront sensor based on an industrial smart camera," *IEEE Transactions on Instrumentation and Measurement*, vol. 62, no. 5, pp. 1241-1249, 2013.
- [17] D. R. Burada, K. K. Pant, M. Bichra, G. S. Khan, S. Sinzinger, and C. Shakher, "Experimental investigations on characterization of freeform wavefront using Shack-Hartmann sensor," *Optical Engineering*, vol. 56, no. 08, p. 1, 2017.
- [18] K. K. Pant, D. R. Burada, M. Bichra, M. P. Singh, A. Ghosh, G. S. Khan, S. Sinzinger, and C. Shakher, "Subaperture stitching for measurement of freeform wavefront," *Applied Optics*, vol. 54, no. 34, p. 10022, 2015.
- [19] M. Rocktäschel and H. J. Tiziani, "Limitations of the Shack-Hartmann sensor for testing optical aspherics," *Optics and Laser Technology*, vol. 34, no. 8, pp. 631-637, 2002.
- [20] M. Fuerst, S. Unger, S. Ito, and G. Schitter, "Wavefront measurement based feedback control for automatic alignment of a high-NA optical system," *Journal of Physics: Conference Series*, vol. 1065, p. 032001, 2018.
- [21] M. E. Fuerst and G. Schitter, "Scanning Wavefront Sensor for Measurement of Highly Divergent Wavefronts," *8th IFAC Symposium on Mechatronic Systems*, vol. 52, no. Mechatronics, pp. 25-30, 2019.
- [22] M. E. Fuerst, N. Berlakovich, E. Csencsics, and G. Schitter, "Self-aligning scanning shack-hartmann sensor for automatic wavefront measurements of high-na optics," in *2020 IEEE International Instrumentation and Measurement Technology Conference (I2MTC)*. IEEE, 2020.
- [23] A. Chernyshov, U. Sterr, F. Riehle, J. Helmcke, and J. Pfund, "Calibration of a Shack-Hartmann sensor for absolute measurements of wavefronts," *Applied Optics*, vol. 44, no. 30, pp. 6419-6425, 2005.
- [24] S. Mauch, S. Member, J. Reger, and S. Member, "Real-Time Spot Detection and Ordering for a Shack - Hartmann Wavefront Sensor With a Low-Cost FPGA," *IEEE Transactions on Instrumentation and Measurement*, vol. 63, no. 10, pp. 2379-2386, 2014.
- [25] G. M. Dai, *Wavefront optics for vision correction Vol. 179*. Bellingham: SPIE press, 2008.
- [26] Z. Pandilov and V. Dukovski, "Comparison of the characteristics between serial and parallel robots," *Acta Technica Corvinensis-Bulletin of Engineering*, vol. 7, no. 1, 2014.
- [27] P. Aerotech Inc., Pittsburgh, "Rotary Stages ABR Series" datasheet, 2020.
- [28] G. PI Physik Instrumente, Karlsruhe, "VT-80 Linear Stage, Basic version for Universal Fields of Use" data sheet, 2020.
- [29] K. K. Pant, D. R. Burada, A. Ghosh, G. S. Khan, and C. Shakher, "Improved subaperture stitching for the measurement of freeform wavefront," in *Optics InfoBase Conference Papers*, vol. Part F114-, 2018, pp. 2-3.



Martin E. Fuerst is pursuing his PhD in the Advanced Mechatronic Systems Group at the Automation and Control Institute (ACIN) of TU Wien. He received an MSc. degree in Biomedical Engineering and an MSc. degree in Physical Measurement Engineering in 2016 and 2017, respectively. His primary research interests are optical wavefront measurement techniques, advances in optical displacement sensing, and optical freeform manufacturing and testing.



measurement systems.

Ernst Csencsics is a postdoctoral researcher in the Advanced Mechatronic Systems Group at the Automation and Control Institute (ACIN) of TU Wien. He received an MSc. and a PhD degree (sub auspiciis) in Electrical Engineering from TU Vienna, Austria in 2014 and 2017, respectively. His primary research interests are on high performance mechatronic systems, the development of holistic methods for multidisciplinary system design and integration, opto-mechatronic measurement and imaging systems, precision engineering, and robot-based in-line



Nikolaus Berlakovich received an MSc degree in Physics from TU Wien in 2016. He is currently pursuing a PhD degree at the Automation and Control Institute (ACIN) of TU Wien. His research interests include algorithms related to high-performance optical metrology, especially for wavefront stitching, and precision engineering for automated in-line metrology.



Georg Schitter is Professor for Advanced Mechatronic Systems at the Automation and Control Institute (ACIN) of TU Wien. He received an MSc in Electrical Engineering from TU Graz, Austria (2000) and an MSc and PhD degree from ETH Zurich, Switzerland (2004). His primary research interests are on high-performance mechatronic systems, particularly for applications in the high-tech industry, scientific instrumentation, and mechatronic imaging systems, such as AFM, scanning laser and LIDAR systems, telescope systems, adaptive optics, and lithography systems for semiconductor industry.

He received the journal best paper award of IEEE/ASME Transactions on Mechatronics (2018), of the IFAC Mechatronics (2008-2010), of the Asian Journal of Control (2004-2005), and the 2013 IFAC Mechatronics Young Researcher Award. He served as an Associate Editor for IFAC Mechatronics, Control Engineering Practice, and for the IEEE Transactions on Mechatronics.